

# Bond Graph Modelling of Chemoelectrical Energy Transduction.

Peter J. Gawthrop<sup>1,\*</sup>, Ivo Siekmann<sup>2</sup>, Tatiana Kameneva<sup>1</sup>, Susmita Saha<sup>3</sup>,  
Michael R. Ibbotson<sup>3,4</sup>, and Edmund J. Crampin<sup>1,5,6</sup>

<sup>1</sup>Department of Electrical and Electronic Engineering, The University of Melbourne, Australia.

<sup>2</sup>Institute for Mathematical Stochastics, University of Göttingen, Germany.

<sup>3</sup>National Vision Research Institute, Australian College of Optometry, Australia.

<sup>4</sup>Centre of Excellence for Integrative Brain Function, Dept. Optometry and Vision Sciences, The University of Melbourne, Australia.

<sup>5</sup>School of Mathematics and Statistics, University of Melbourne University of Melbourne, Victoria 3010, Australia

<sup>6</sup>School of Medicine, University of Melbourne, Victoria 3010, Australia

\*Corresponding author: [peter.gawthrop@unimelb.edu.au](mailto:peter.gawthrop@unimelb.edu.au)

April 20, 2017

## Abstract

Energy-based bond graph modelling of biomolecular systems is extended to include chemoelectrical transduction thus enabling integrated thermodynamically-compliant modelling of chemoelectrical systems in general and excitable membranes in particular.

Our general approach is illustrated by recreating a well-known model of an excitable membrane. This model is used to investigate the energy consumed during a membrane action potential thus contributing to the current debate on the trade-off between the speed of an action potential event and energy consumption. The influx of  $\text{Na}^+$  is often taken as a proxy for energy consumption; in contrast, this paper presents an energy based model of action potentials. As the energy based approach avoids the assumptions underlying the proxy approach it can be directly used to compute energy consumption in both healthy and diseased neurons.

These results are illustrated by comparing the energy consumption of healthy and degenerative retinal ganglion cells using both simulated and *in vitro* data.

# Contents

<b>1</b>	<b>INTRODUCTION</b>	<b>3</b>
<b>2</b>	<b>MODELLING APPROACH</b>	<b>5</b>
<b>3</b>	<b>Bond Graph Modelling of Voltage Gating</b>	<b>12</b>
<b>4</b>	<b>Energy Flow in the Hodgkin Huxley Action Potential</b>	<b>17</b>
<b>5</b>	<b>Energy consumption in healthy and degenerative retinal ganglion cells</b>	<b>21</b>
<b>6</b>	<b>DISCUSSION</b>	<b>23</b>
<b>7</b>	<b>ACKNOWLEDGEMENTS</b>	<b>25</b>
<b>8</b>	<b>AUTHOR CONTRIBUTIONS</b>	<b>25</b>
<b>9</b>	<b>DATA ACCESSIBILITY</b>	<b>25</b>
<b>10</b>	<b>References</b>	<b>25</b>
<b>A</b>	<b>Application of the proposed methodology to calculate the energy consumption in healthy and degenerative retinal ganglion cells</b>	<b>30</b>

# 1 INTRODUCTION

Energy is fundamental to science in general and the life sciences in particular [1]. For this reason, the energy-based bond graph modelling method, originally developed in the context of engineering [2], has been applied to modelling biomolecular systems [3–8]. Bond graphs represent the energy consumption per unit time, or power flow, for each component of a given system. Power flows are calculated as the product of appropriately chosen ‘signal quantities’ named ‘efforts’ and ‘flows’. Examples of effort include force, voltage, pressure and chemical potential. Corresponding examples of flow are velocity, current, fluid flow rate and molar flow rate. By describing systems under the unifying principle of energy flows and due to the abstract representation of these flows in terms of generalised effort and flow quantities, the bond graph approach is particularly appropriate for modelling systems with multiple energy domains. A comprehensive account of the use of bond graphs to model engineering systems is given in the textbooks of Gawthrop and Smith [9], Mukherjee et al. [10], Borutzky [11] and Karnopp et al. [12] and a tutorial introduction for control engineers is given by Gawthrop and Bevan [13]. Chemical reactions are considered by Cellier [14] and Greifeneder and Cellier [15]. In particular, as an engineering example, Karnopp [16] has looked at chemoelectrical energy flows in hybrid vehicles.

Chemoelectrical energy transduction is fundamental to living systems and occurs in a number of contexts including oxidative phosphorylation and chemiosmosis, synaptic transmission and action potentials in excitable membranes. For this reason, this paper extends the energy-based bond graph modelling of biomolecular systems to biological systems which involve chemoelectrical energy transduction. A simple model of the action potential in excitable membranes is used as an illustrative example of the general approach. Although such simple models could easily be derived by other means, our general approach could be used to build thermodynamically compliant models of large hierarchical systems such as those describing metabolism, signalling and neural transmission.

Understanding the biophysical processes which underlie the generation of the action potential in excitable cells is of considerable interest, and has been the subject of intensive mathematical and computational modelling. Since the early work of Hodgkin and Huxley [17] on modelling the ionic mechanisms which give rise to the action potential in neurons, mathematical models of the action potential have incorporated ever-increasing biophysical and ionic detail [18], and have been formulated to describe both normal and pathophysiological mechanisms. Generation of the action potential comes at a metabolic cost. Energy is required to maintain the imbalance of ionic species across the membrane, such that when ion channels open there is a flux of ions (current) across the membrane – initially carried by sodium ions – generating rapid membrane depolarisation (the upstroke of the action potential). Each action potential reduces the ionic imbalance and each ionic species needs to be transported across the membrane against an adverse electrochemical gradient to restore the imbalance – this requires energy.

The role of energy in neural systems has been widely discussed in the literature [19–25] and it has been suggested that metabolic cost is a unifying principle underlying the functional organisation and biophysical properties of neurons [21, 26]. Furthermore, Beal [27] posed the question “Does impairment of energy metabolism result in excitotoxic neuronal death in neurodegenerative illnesses?” More recently, it has been suggested [28–31] that an

energy-based approach is required to elucidate neurodegenerative diseases such as Parkinson’s disease.

In such studies, the flow of  $\text{Na}^+$  across the membrane is taken as a proxy for energy consumption associated with action potential generation, as  $\text{Na}^+$  has to be pumped back across the membrane by an energy-consuming ATPase reaction. This energetic cost is often quoted as an equivalent number of ATP molecules required to restore the ionic concentration gradient through activity of the sodium-potassium ATPase (the Na pump), as calculated via stoichiometric arguments. While this provides a useful indication of energetic cost, this is however an imprecise approach, which cannot produce reliable estimates of energy flows under all conditions (physiological and pathophysiological). What is required instead is a way of simulating and calculating the actual energy flows associated with these ionic movements through a physically-based modelling approach.

Here we develop a general bond graph based modelling framework that enables explicit calculation of the energy flows involved in moving ions across the cell membrane. Our model can be applied to the regulation of the membrane potential via ion channels in any cell type—obvious examples include, for example, cardiac and skeletal muscle cells—but in order to give a specific application we investigate the energy cost for generating a neural action potential. Because ions carry electrical charge, differences in the concentration of a particular ionic species on either side of a membrane generate both a chemical potential difference due to the concentration gradient as well as an electrical potential difference due to charge imbalance.

The Hodgkin-Huxley model [17] is used throughout this paper as a well-known and well-documented exemplar to illustrate our approach; however the approach is equally valid for more recent models. In particular, we derive a bond graph formulation focusing on the flow of energy associated with voltage-dependent ionic membrane flow and this formulation encompasses both the classical Hodgkin-Huxley model and more recent models.

One component of this formulation accounts for the behaviour of the ion channel as an electrical resistor that can be investigated experimentally via current-voltage relationships, also known as  $I$ - $V$  curves. Popular models for  $I$ - $V$  curves are, for example, the linear  $I$ - $V$  dependency that corresponds to Ohm’s law and the non-linear Goldman-Hodgkin-Katz (GHK) equations. Hodgkin-Huxley-like models assume a linear  $I$ - $V$  relationship. Hodgkin and Huxley [17] represented the voltage-dependent opening and closing of ion channels by an empirical model, their gating variables, which led to excellent agreement with experimental data. This paper replaces this empirical model of gating by an physically-based voltage-dependent Markov model with one open and one closed state. Whereas this model accounts for the energy needed for moving the ion channel between conformations where the channel is in an open or a closed state, respectively, the empirical gating variables of the Hodgkin-Huxley model do not have a similar interpretation.

As our models are formulated using bond graphs, important physical quantities such as mass and energy are conserved (in the sense that any dissipative processes are directly accounted for, and any inputs to or losses from the system are quantified).

This theoretical approach is then applied to analyse energy consumption in retinal ganglion cells based on *in vitro* experimental data collected and analysed from retinal ganglion cells (RGCs) of wild-type (WT) and degenerative (RD1) mice. Our use of the RD1 degenerate retina mouse model ensures that the outcomes of this project are directly relevant to



A bond graph representation of (1) according to the framework developed by Gawthrop and Crampin [5] is given in Figure 1. Using this specific example we briefly review the bond graph approach developed in our previous work. The components of a bond graph are distinguished based on how they transform energy. Capacitors or springs store energy (**C**), resistors or dampers dissipate energy (**R**), and transducers (or transformers) (**TF**) which transmit and convert, but do not dissipate, power. The chemical species appearing in (1) are represented in the bond graph by capacitors **C**: $x_i$ , **C**: $x_e$ , **C**: $P$  and **C**: $G$ . Because a given type of component usually occurs more than once in a given system, the ‘colon’ notation is adopted to distinguish between different instances of each component type: the symbol preceding the colon identifies the type of component, and the label following the colon identifies the particular instance.

Let us first consider the species  $x_i$  and  $x_e$ . These are simply the concentrations of a particular ion within the cell ( $x_i$ ) and outside the cell ( $x_e$ ) so that their rates of change must equal the molar flow rate  $v_{ion}$  in  $\text{mol s}^{-1}$  with opposite sign:

$$\dot{x}_i = -v_{ion}, \quad \dot{x}_e = v_{ion}. \quad (2)$$

It is assumed that in the body biochemical reactions occur under conditions of constant pressure (isobaric) and constant temperature (isothermal). Under these conditions, the chemical potential  $\mu_A$  of substance  $A$  measured in  $\text{J mol}^{-1}$  is given [1] in terms of its mole fraction  $\chi_A$  as:

$$\mu_A = \mu_A^* + RT \ln \chi_A \quad (3)$$

where  $\mu_A^*$  is the value of  $\mu_A$  when  $A$  is pure ( $\chi_A = 1$ ),  $R = 8.314 \text{ J K}^{-1} \text{ mol}^{-1}$  is the universal gas constant,  $T \text{ K}$  is the absolute temperature and  $\ln$  is the natural (or Napierian) logarithm. By introducing the *thermodynamic constant*  $K_A$

$$K_A = \frac{1}{n_{total}} \exp \frac{\mu_A^*}{RT} \quad (4)$$

where  $n_{total}$  is the total number of moles in the mixture we can express the chemical potential as a function of molar amount  $x_A$  of the species  $A$ :

$$\mu_A = RT \ln K_A x_A. \quad (5)$$

As discussed by Oster et al. [3, 4] the chemical potential  $\mu$  and the molar flow  $v$  are appropriate *effort* and *flow* variables for modelling chemical reactions. The product of chemical potential  $\mu$  and molar flow  $v$  is the energy flow into the bond graph **C** components and has the unit  $\text{J s}^{-1}$  of *power*. This is shown in Figure 1 by power bonds (or more simply ‘bonds’), drawn as harpoons:  $\rightarrow$ . These bonds can optionally be annotated with specific effort and flow variables, for example  $\frac{e}{f}$ . The half-arrow on the bond indicates the direction in which power flow will be regarded as positive and thus defines a sign convention. As explained above, for the components **C**: $x_i$  and **C**: $x_e$  we have the flows  $-v_{ion}$  and  $v_{ion}$ ,

respectively, and the chemical potentials are [5]:

$$\mu_i = RT \ln K_i x_i \quad (6)$$

$$\mu_e = RT \ln K_e x_e \quad (7)$$

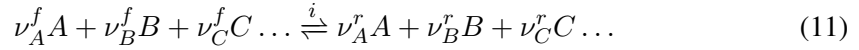
$$\text{where } K_i = \frac{K_{ion}}{C_i} \quad (8)$$

$$\text{and } K_e = \frac{K_{ion}}{C_e} \quad (9)$$

$$\text{where } K_{ion} = \exp \frac{\mu^0}{RT} \quad (10)$$

$\mu^0$  is the standard chemical potential for the ion and the volumetric capacities of the interior and exterior are  $C_i$  and  $C_e$ , respectively. In general, bond graph components which are connected by a bond share the same effort and flow. Thus, because all energy flows between bond graph components are quantified, the bond graph ensures that properties such as energy and mass are conserved.

We follow Oster et al. [4] in describing chemical reactions in terms of the *Marcelin – de Donder* formulae as discussed by Van Rysselberghe [33] and Gawthrop and Crampin [5]. In particular, given the  $i$ th reaction [4, (5.9)]:



where the stoichiometric coefficients  $\nu$  are either zero or positive integers and the *forward affinity*  $A_i^f$  and the *reverse affinity*  $A_i^r$  are defined as:

$$A_i^f = \nu_A^f \mu_A + \nu_B^f \mu_B + \nu_C^f \mu_C \dots \quad (12)$$

$$A_i^r = \nu_A^r \mu_A + \nu_B^r \mu_B + \nu_C^r \mu_C \dots \quad (13)$$

Thus, the affinities  $A_i^f$  and  $A_i^r$  are sums of the chemical potentials appearing on either side of (11) weighted with the stoichiometric coefficients  $\nu$ . In a bond graph model, the affinities from (12), (13) can be obtained via a ‘**1** junction’. Junctions allow parallel (‘**0**’ junction) and series (‘**1**’ junction) connections to be made. The efforts on bonds impinging on a **1** junction sum to zero whereas the flows are all equal (this is equivalent to Kirchhoff’s second law for electrical circuits, where effort is equivalent to voltage and flow is equivalent to current). Analogously, for a **0** junction the flows sum to zero and the efforts are all equal (equivalent to Kirchhoff’s first law). Taking into account the sign convention explained above it is easy to see that  $A^f$  and  $A^r$  in Figure 1 are indeed weighted sums of chemical potentials as in (12), (13):

$$A^f = A^g(V) + \mu_i + \mu_V \quad (14)$$

$$A^r = A^g(V) + \mu_e \quad (15)$$

The affinity of the gating species  $A^g(V)$  as well as the potential  $\mu_V$  of the electrogenic species will be derived further below.

The Marcelin – de Donder formulae enable us to calculate the flow of a reaction for which we assume the law of mass action from the affinities:

$$v_i = \kappa_i (v_0^+ - v_0^-) \quad (16)$$

$$\text{where } v_0^+ = e^{\frac{A_i^f}{RT}} \text{ and } v_0^- = e^{\frac{A_i^r}{RT}} \quad (17)$$

Note that the arguments of the exponential terms are dimensionless as are  $v_0^+$  and  $v_0^-$ . The units of the reaction rate constant  $\kappa_i$  are those of molar flow rate:  $\text{mol sec}^{-1}$ .

The flow  $v_i$  is obtained from the efforts  $A_i^f$  and  $A_i^r$ , similar to an electrical resistor where Ohm's law requires that the current is proportional to the potential difference across the resistor. In contrast to the linear electrical **R** component, the non-linear effort-flow relationship of (16) can be represented by a two port resistive component, the **Re** component [5]. Resistive components such as **R** and **Re** components dissipate energy.

So far we have not accounted for the interdependency of the molar flow  $v_{ion}$  and the electrical potential  $V$  across the cell membrane. As discussed in bond graphs terms by [16] the well-known physical relationship between the molar flow of ions  $v_{ion}$  across the membrane and the current  $i$

$$i = zFv_{ion} \quad (18)$$

in fact describes the coupling of two energy domains, namely chemical energy and electrical energy. Here  $z$  is the (integer) ionic charge and  $F$  Faraday's constant which has the approximate value  $F \approx 96.5 \times 10^3 \text{C mol}^{-1}$ . Thus, for example, an ion with unit charge and flow rate of  $1 \text{ nmol sec}^{-1}$  is equivalent to a current of about  $96.5 \mu \text{A}$ .

Using the bond graph *transformer* element denoted by **TF**, equation (18) enables us to associate a *chemoelectrical potential*  $\mu_V$  with an ionic current  $i$  at a membrane potential  $V$ . As shown in Figure 2(a), the transformer **TF:zF** converts electrical power  $V_Q i$  to chemical power  $\mu_V v_{ion}$  so that from  $V_Q i = \mu_V v_{ion}$  we can derive the defining equation of the chemoelectrical potential

$$\mu_V = zFV_Q \quad (19)$$

Thus, for example, a voltage of  $1 \text{ mV}$  is equivalent to a chemical potential of an ion with unit charge of about  $96.5 \text{ J mol}^{-1}$

Stoichiometric analysis of biochemical reactions has a bond graph interpretation in terms of the bond graph structure. As a structural matrix, the stoichiometric matrix for biochemical systems contains integer entries corresponding to reaction stoichiometry. The bond graph describing chemoelectrical transduction in Figure 2(a) contains transformers connecting the electrical and chemical domains and the chemoelectrical transformer contains the Faraday constant  $F$  which is not an integer. For this reason, it is useful as shown in Figure 2(b) to split the component **TF:zF** into two **TF** components in series: **TF:z** and **TF:F**. Thus **TF:z** corresponds to the integer, but ion-dependent charge,  $z$ , and **TF:F** to the universal constant, but non-integer,  $F$ . **TF:z** will be referred to as the *electrostoichiometric transformer* with ratio  $z$ . With reference to Figures 2(b)&(c)

$$v = zv_{ion} \quad \mu_V = z\mu_Q \quad (20)$$

Furthermore, the electrical component **C:Q** and the chemoelectrical transformer **TF:F** component may be replaced by a single *electrogenic capacitor* **C:P** as in Figure 2(c). As-



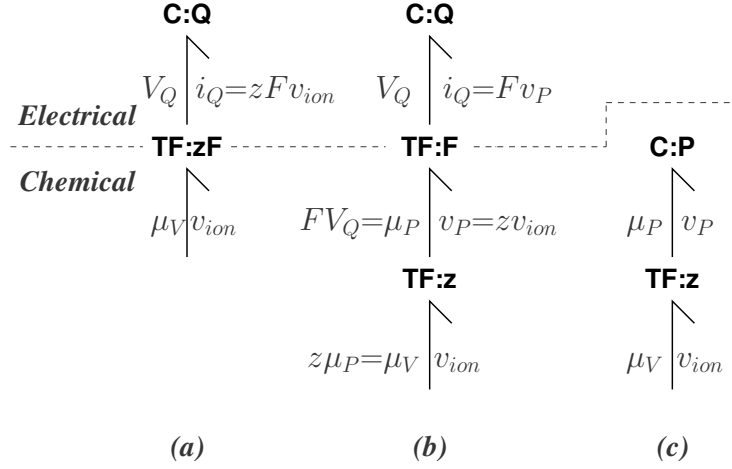


Figure 2: Chemoelectrical Transduction. (a) The transduction of ion membrane flow  $v_{ion}$  into electrical current  $i$  is represented by **TF:zF** where  $z$  is the ionic charge and  $F$  Faraday's constant; **C:Q** represents the membrane capacitance containing electrical charge  $Q$  and  $\mu_V$  is the *chemoelectrical potential*: the chemical potential corresponding to the membrane voltage  $V$  (b) **TF:zF** is split into two series components **TF:z** & **TF:F**. (c) The electrical capacitor **C:Q** and the chemoelectrical transducer **TF:F** are combined into chemo-equivalent capacitor **C:P** containing  $x_m$  moles of charge. **C:P** is analogous to a chemical species, and **TF:z** to a stoichiometric transformer.

suming that the electrical capacitor has the constant capacitance  $C$  ( $\text{CV}^{-1}$ ), and with reference to Figure 2(b)

$$\mu_Q = FV_Q \quad V_Q = \frac{Q}{C} \quad \dot{Q} = i_Q \quad i_Q = Fv_P \quad (21)$$

While the electrogenic capacitor **C:P** is linear and therefore cannot be written in the logarithmic form of Equation (5), it is convenient to write the defining equations in a similar form by defining the number of moles of charge  $x_m$  as

$$x_m = \frac{Q}{F} \quad (22)$$

With reference to Figure 2(c)

$$\mu_P = RTK_e x_m \quad \dot{x}_m = v_P \quad (23)$$

Comparing Equations (21) and (23), it follows that:

$$K_e = \frac{F^2}{CRT} = \frac{V_e}{V_N} \text{mol}^{-1} \quad (24)$$

where  $V_e = \frac{F}{C} \text{Vmol}^{-1}$  and  $V_N = \frac{RT}{F} \text{V}$

$V_e$  is the *equivalent voltage* associated with each mole of charge and is dependent on the electrical capacitance  $C$ .  $V_N$  is related to the *Nernst potential* and is temperature dependent.

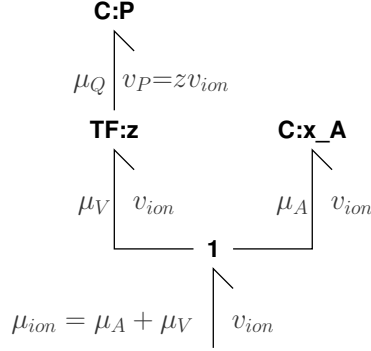


Figure 3: Combined chemoelectrical and chemical potentials

In summary, **C:P** is analogous to a chemical species (but with a non-logarithmic characteristic), and **TF:z** is analogous to the stoichiometric transformers discussed by Oster et al. [3, 4], Greifeneder and Cellier [15] and Gawthrop and Crampin [5]. Because the influence of the membrane potential  $V$  can be translated to the contribution of the electrogenic species, its effect on the flow of a species  $A$  can be accounted for in the bond graph just like a reaction of two normal species by coupling the efforts  $\mu_V$  and  $\mu_A$  via a **1** junction [5] as shown in Figure 3. From the bond graph representation we rederive the standard electrostatic contribution to the chemoelectrical potential:

$$\mu_{ion} = \mu_A + \mu_V = \mu_A + z\mu_Q = \mu_A + zFV_Q = \mu_A + FV \quad (25)$$

In general, as discussed below, the electrogenic capacitor will correspond to the net flow of more than one charged species.

Similar to our approach to modelling the membrane potential we will also represent the voltage-dependent gating of ion channels as a chemical species. In this way we obtain a general model for ionic flow through ion channels across cell membranes. We will demonstrate that our general model of voltage-dependent gating includes the original Hodgkin-Huxley model and its extensions beyond sodium  $\text{Na}^+$ , potassium  $\text{K}^+$  and leak currents. As a specific application of our framework we will investigate the energy flow related to the action potential predicted by Hodgkin-Huxley like models. Our analysis clarifies that the phenomenological gating variables introduced by [17] fail to account appropriately for energy flows related to ion channel gating.

As shown in the chemical reaction (1) that our model is based upon, the *gating species*  $G$  behaves like an enzyme that catalyses the conversion of the intracellular species  $X_i$  to the extracellular species  $X_e$ . In the same way as in Gawthrop and Crampin [5, Figure 2e] the *gating affinity*  $A^g$  is added to both sides of the reaction (Figure 1). The second port **SS:[g]** imposes the gating affinity  $A^g$  and the corresponding flow  $v_g = v_{ion} - v_{ion} = 0$ . With the gating affinity

$$A^g = \mathbf{RT} \ln G_{pore}(V) + \mathbf{RT} \ln G_{ion}(V) \quad (26)$$

$$\text{or } \exp(A^g/\mathbf{RT}) = G_{pore}(V)G_{ion}(V) \quad (27)$$

we represent two characteristics of the ionic flow through a channel. The term  $G_{pore}(V)$  accounts for the fact that an ion channel has an electrical resistance that opposes the ionic

current. The electrical resistance is commonly investigated experimentally by determining current-voltage relationships. It will be demonstrated that the two most commonly used models for current-voltage relationships of ion channels, Ohm's law and the Goldman-Hodgkin-Katz (GHK) equations, can be obtained by suitable choices of  $G_{pore}(V)$ . Whereas  $G_{pore}(V)$  represents the conductance through an open channel,  $G_{ion}(V)$  provides a model for the voltage-dependent opening and closing of the channel. From Equations (12-16) we obtain our model for the ionic flow through an ion channel:

$$v_{ion} = \kappa \left[ \exp \left( \frac{A^g(V) + \mu_i + \mu_V}{RT} \right) - \exp \left( \frac{A^g(V) + \mu_e}{RT} \right) \right] \quad (28)$$

$$= \kappa K_{ion} \exp A^g(V) (c_i \exp \bar{V} - c_e) \quad (29)$$

$$\text{where } c_i = \frac{x_i}{C_i}, c_e = \frac{x_e}{C_e}, V_N = \frac{RT}{F} \text{ and } \bar{V} := \frac{V}{V_N} \quad (30)$$

Define  $\bar{V}_{ion}$  as the voltage for which  $v_{ion}$  of Equation (29) is zero:

$$c_i \exp \bar{V}_{ion} - c_e = 0 \quad (31)$$

$$\text{hence } \bar{V}_{ion} = \ln \frac{c_e}{c_i} = -\ln \frac{c_i}{c_e} \quad (32)$$

Using Equations (32) and (27), Equation (29) becomes:

$$v_{ion} = \kappa K_{ion} c_e G_{ion}(V) G_{pore}(V) (\exp \tilde{V}_{ion} - 1) \quad (33)$$

where  $\tilde{V}_{ion}$  is given by

$$\tilde{V}_{ion} = \frac{V - V_{ion}}{V_N} = \bar{V} - \bar{V}_{ion}. \quad (34)$$

The quantity  $\exp(-\tilde{V}_{ion})$  is known as the *Ussing Flux Ratio* [34, §3.2]. The ionic flow (ion current) model of Equation (33) will be used in the sequel to construct a Bond Graph model from the Hodgkin Huxley model.

Hodgkin and Huxley [17] model an ion channel according to Ohm's law i.e. as a linear conductance  $g_{ion}$ , modulated by a function  $G_{ion}$  in series with the Nernst potential represented by a voltage source  $V_{ion}$  (see Figure 4).

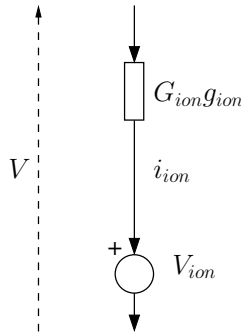


Figure 4: The Hodgkin-Huxley Axon Model

$$i_{ion} = g_{ion} G_{ion}(V, t) (V - V_{ion}) \quad (35)$$

where  $0 \leq G_{ion}(V, t) \leq 1$  is the gating function, which is a dynamic function of membrane potential  $V$ . In terms of ionic flow  $v_{ion}$ , Equation (35) becomes, using (34):

$$\begin{aligned} v_{ion} &= \frac{1}{F} i_{ion} = \frac{g_{ion} G_{ion}(V, t) V_N}{F} \tilde{V}_{ion} \\ &= \kappa_{HH} c_e G_{ion}(V, t) \tilde{V}_{ion} \end{aligned} \quad (36)$$

$$\text{where } \kappa_{HH} = \frac{g_{ion} V_N}{F c_e} \quad (37)$$

It is easy to see that our model (33) contains the Hodgkin-Huxley model (36) by a suitable choice of  $G_{pore}$ :

$$G_{pore} = G_{HH}(V) = \begin{cases} 1 & \tilde{V} = 0 \\ \frac{\tilde{V}_{ion}}{\exp \tilde{V}_{ion} - 1} & \tilde{V}_{ion} \neq 0 \end{cases} \quad (38)$$

Clearly, equation (38) only makes sense if  $G_{HH}$  is positive for all  $\tilde{V}$ . If  $\tilde{V} < 0$ , both  $\tilde{V}$  and  $\exp \tilde{V} - 1$  are negative; if  $\tilde{V} > 0$ , both  $\tilde{V}$  and  $\exp \tilde{V} - 1$  are positive; and, as  $G_{HH}(0) = 1$ ,  $G_{HH}(\tilde{V})$  is positive for for all  $\tilde{V}$ .

A number of alternative physically-based models for the ion channel are available. In particular, the Goldman-Hodgkin-Katz (GHK) model (see Keener and Sneyd [34, § 2.6.3 (2.123)], Koch [35, § 9.1.1]) & Sterratt et al. [36] can be rewritten in a similar form to (33) as:

$$v = \kappa K_0 c_e \bar{V} \frac{\exp \tilde{V} - 1}{\exp \bar{V} - 1} \quad (39)$$

Comparing Equations (33) and (39), it follows that the mass action model (33) and GHK model are the same if the model-dependent function  $G_{pore}(V)$  is:

$$G_{pore} = G_{GHK}(V) = \begin{cases} 1 & \bar{V} = 1 \\ \frac{\bar{V}}{\exp \bar{V} - 1} & \bar{V} \neq 1 \end{cases} \quad (40)$$

Note that  $G_{GHK}(V)$  (40) is of the same form as  $G_{HH}(V)$  (38) except that  $\tilde{V}$  is replaced by  $\bar{V}$ .

From equations (36) and (33), both the HH and GHK ion channel models give zero ionic flow when the membrane voltage equals the Nernst voltage: that is the models match at  $\tilde{V}_{ion} = 0$ . Moreover, the GHK model of Equation (39) has a parameter  $\kappa$  that can be chosen to fit the data. In this case,  $\kappa$  is chosen so that the GHK and HH models also match at another voltage; in this case chosen as minus the Nernst voltage. Figure 5 shows the ionic currents plotted against membrane voltage for the  $K^+$  and  $Na^+$  channels and they match at the two voltages. The GHK model is used in the sequel.

### 3 Bond Graph Modelling of Voltage Gating

Up to this point our general energy-based framework for ionic transport is consistent with the Hodgkin-Huxley (HH) model. However, our energy-based approach and the HH model

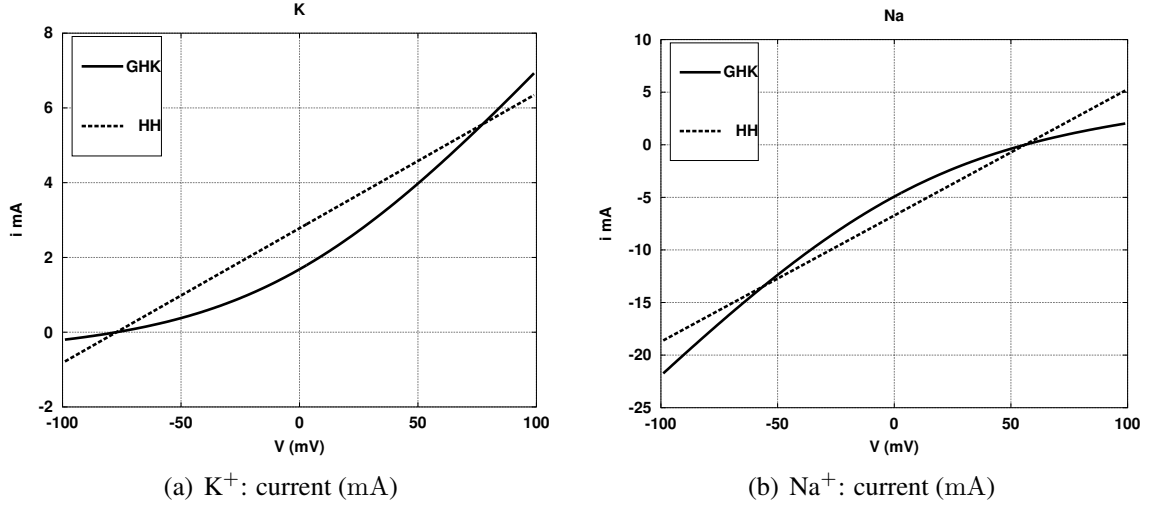


Figure 5: Comparison of current(mA)–voltage(mV) relationships for Na<sup>+</sup> and K<sup>+</sup> currents for  $G_{pore} = G_{HH}$  and  $G_{pore} = G_{GHK}$  models.

Ion	K <sup>+</sup>	Na <sup>+</sup>	Leakage
$\kappa \text{ nmol sec}^{-1}$	0.046262	0.13204	0.0014329

Table 1: GHK parameter  $\kappa \text{ nmol sec}^{-1}$

differ in the description of voltage-dependent gating. With the gating function  $G_{ion}$  we represent the proportion of open channels. As explained by Keener and Sneyd [34],  $G_{ion}$  may depend on one or more so-called gating variables which can be interpreted mechanistically as a model for an ion channel consisting of multiple subunits or gates. The subunits are assumed to open and close independently and for the channel to be open all subunits must be in an open state. According to this interpretation, the K<sup>+</sup> channel of the HH model with

$$G_{K^+} = n^4 \quad (41)$$

consists of four identical subunits whereas the Na<sup>+</sup> channel with

$$G_{Na^+} = m^3 h \quad (42)$$

consists of three subunits of one and a single subunit of another type. The gating variables are all represented by linear first-order differential equations with voltage-dependent coefficients of the form:

$$\frac{dg}{dt} = \alpha(V)(1 - g) - \beta(V)g \quad (43)$$

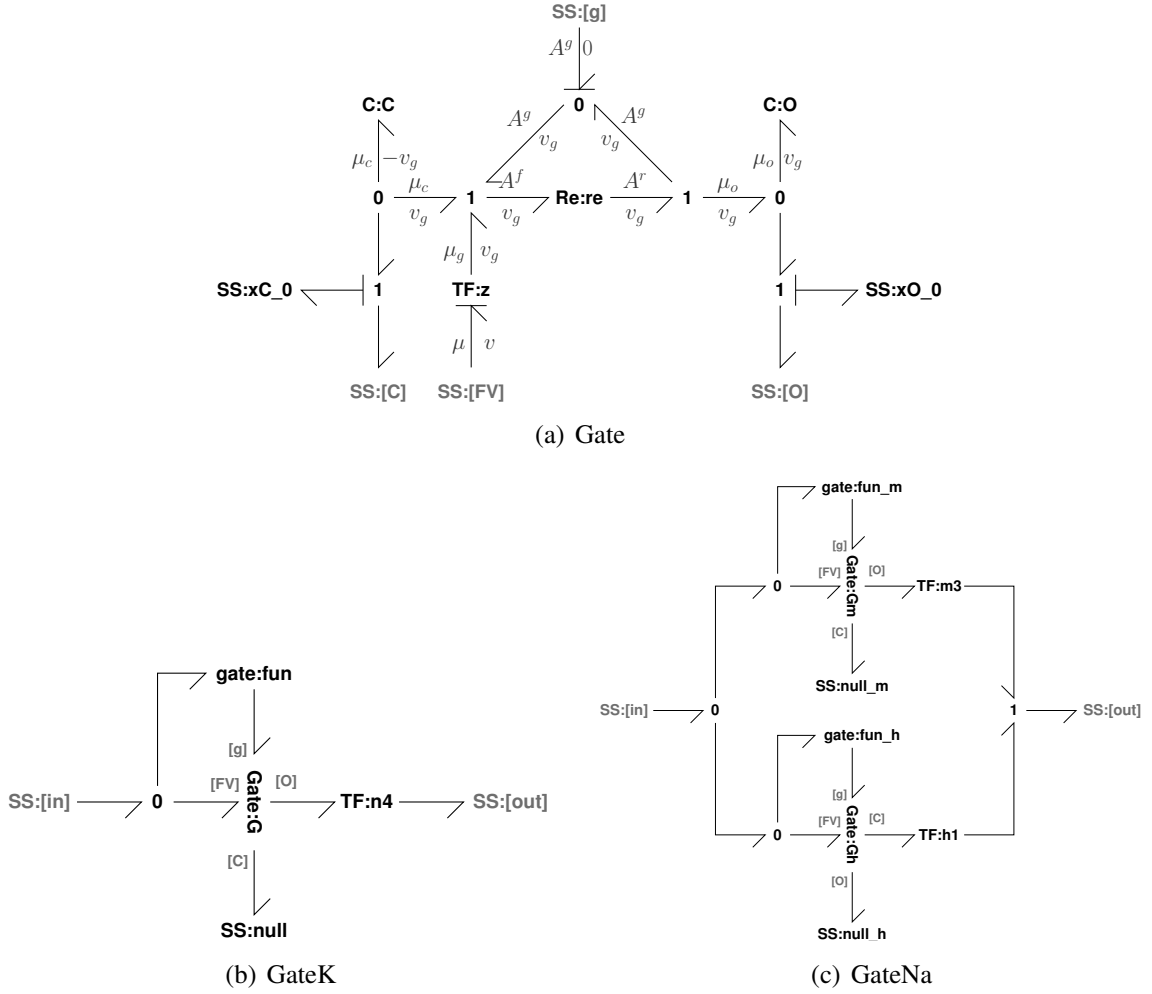


Figure 6: Bond Graph model for physically-plausible gating. (a) The voltage-modulated gate is modelled in a similar way the the ion channel of Figure 1. (b) The basic gate of (a) is used in the  $K^+$  gate. The open state is used and the closed state discarded. The gate equations (43) are implemented in **gate** and the  $n^4$  factor by **TF:n4**. (c) The basic gate of (a) is used in the  $Na^+$  gate. There are separate models for the  $m$  and  $h$  gates. The  $m^3$  factor by **TF:m3**.

This can be rewritten in a more convenient form as:

$$\frac{dg}{dt} = -\tau(V) (g_{ss}(V) - g) \quad (44)$$

$$\text{where } \tau(V) = \frac{1}{\alpha(V) + \beta(V)} \quad (45)$$

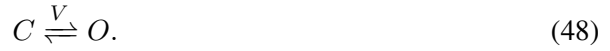
$$\text{and } g_{ss}(V) = \frac{\alpha(V)}{\alpha(V) + \beta(V)} \quad (46)$$

By interpreting (43) as the equation for the open probability of a two-state Markov model with one open and one closed state, the gating variable  $g$  can be regarded—by averaging over many gates—as the proportion of open gates in a population of gates.

In the context of our energy-based framework we now have to determine under which circumstances voltage-dependent two-state Markov models of the form (43) that are used for each gate appearing in the HH model can be given a physical interpretation that enables us to keep track of the energy dissipated by the movement of ions via opening and closing of the gate. As discussed by Keener and Sneyd [34, §3.5] and Hille [18, Chapter 2], it is possible to represent ion channel gates as a set of chemical equations incorporating *gating charge* and *gating current*. This means that the voltage-dependent transitions of a number of gates

$$x_g = x_c + x_o \quad (47)$$

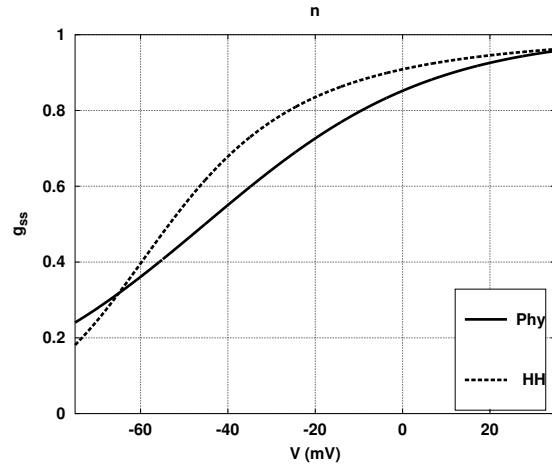
between open and closed states are described as the first-order reaction



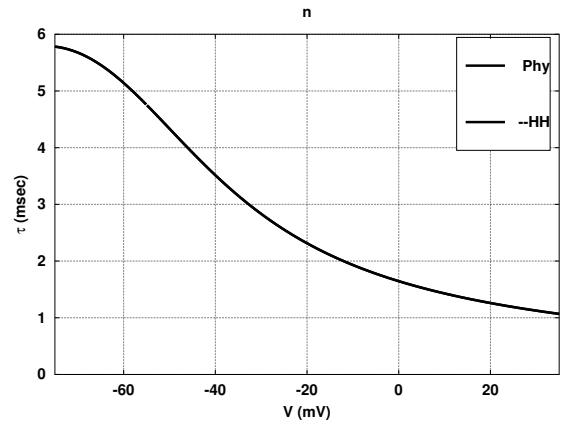
Because (48) has the same structure as the chemical reaction (1) we can derive our model for voltage-dependent gating from the bond graph shown in Figure 6(a) which is completely analogous to Figure 1. From the bond graph of Figure 6(a) we obtain the molar flow

$$\begin{aligned} v_g &= \frac{1}{x_g} \kappa(V) \left( e^{\frac{V}{V_g}} k_c x_c - k_o x_o \right) \\ &= \kappa(V) \left( e^{\frac{V}{V_g}} k_c \left( 1 - \frac{x_o}{x_g} \right) - k_o \frac{x_o}{x_g} \right) \end{aligned} \quad (49)$$

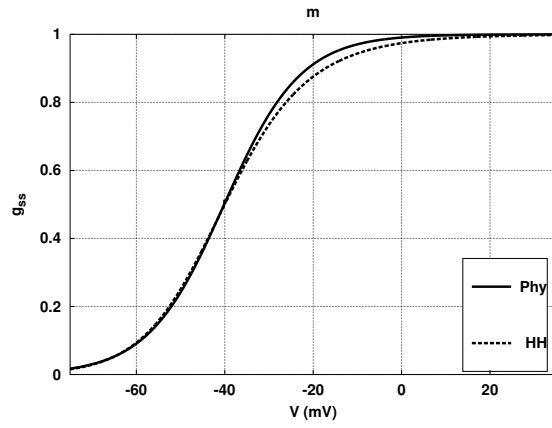
By comparison with the model for the gating variables this shows that the reason why the HH model is not thermodynamically compliant is that we cannot choose the voltage-dependent rates  $\alpha(V)$  and  $\beta(V)$  arbitrarily. In order to compare our approach with the HH model we choose the parameters  $V_g$ ,  $k_c$ ,  $k_o$  and the voltage-dependent rate constants  $\kappa(V)$  for each gate so that it mimics the HH model as closely as possible. This is illustrated for the three gates (n,m,h) used by Hodgkin and Huxley [17] as listed by Keener and Sneyd [34], Equations 5.24–5.29, where the Bond Graph parameters have been chosen to fit the empirical HH model of the form of Equation (43) or (44). Figures 7(a), 7(c) and 7(e) show  $g_{ss}$  for each of the three gates and for both the physical and empirical values. The fit is not exact, as there is no equivalence between the physical gating model and the Hodgkin Huxley empirical model. Figures 7(b), 7(d) and 7(f) show  $\tau$  for each of the three gates and for both the physical and empirical values;  $\kappa(V)$  has been chosen to give an exact fit by making incorporating the empirical expressions for  $\alpha$  and  $\beta$ .



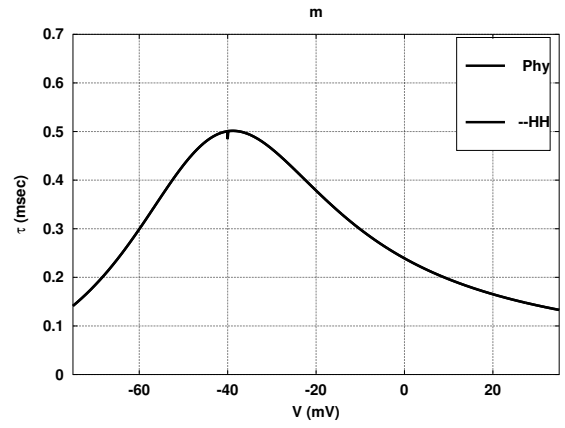
(a) n-gate  $g_{ss}$



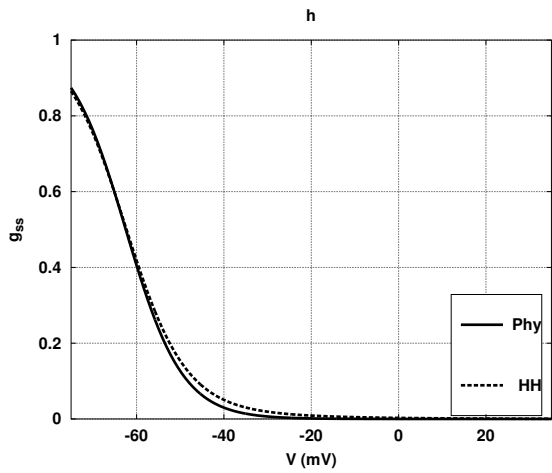
(b) n-gate  $\tau$



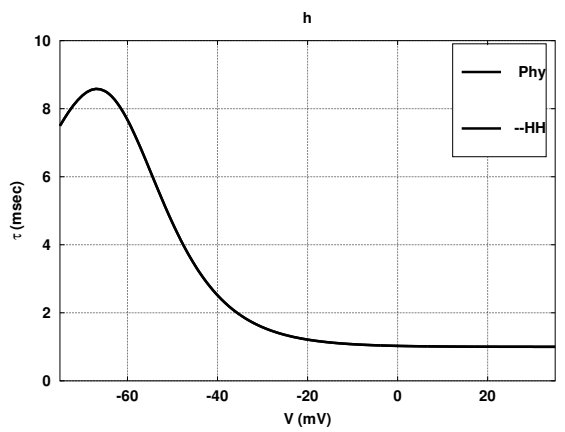
(c) m-gate  $g_{ss}$



(d) m-gate  $\tau$



(e) h-gate  $g_{ss}$



(f) h-gate  $\tau$

Figure 7: Physical Gate Models fitted to Hodgkin-Huxley equations.



It is worth noting that our framework does not rely on the specific gating function  $G_{ion}$  chosen here for comparing an energy-based model approach with the HH model. Parameter values for the Bond Graph gating models are given in Table 2. Unlike the HH model, the gates themselves draw current from the membrane. The amount of current is partly determined by the total gate states  $x_g$ . As the HH model contains no information about gate current, the total gate states  $x_g$  are chosen to give a small, but otherwise arbitrary, value.

Parameter	n	m	h
$z_g$	1	3	4
$k_c$	5.7537	105.49	1
$k_o$	1	1	$6.3281 \times 10^{-5}$
$x_g$	$10^{-9}$	$10^{-9}$	$10^{-9}$

Table 2: Physical-model parameters

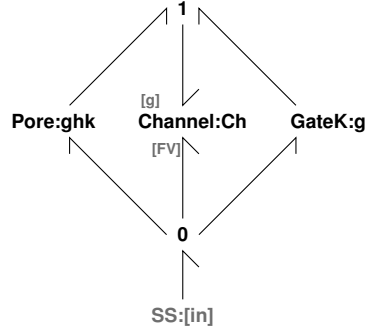


Figure 8: Goldman-Hodgkin-Katz  $K^+$  Channel Model. The  $Na^+$  model is identical except that the right-hand component is replaced by the appropriate gate component. Following the Hodgkin-Huxley model, the leak component is not voltage gated and the right-hand component does not appear. Alternatives to the Goldman-Hodgkin-Katz model are simply obtained by replacing the pore component.

## 4 Energy Flow in the Hodgkin Huxley Action Potential

We are now in a position to reimplement the Hodgkin and Huxley [17] model as a physically-plausible model using the bond graph formulation. As mentioned in the Introduction, the Hodgkin-Huxley model is used here as an exemplar and the general formulation of the rest of this section is equally applicable to other more recent models. Following the interpretation of the model of Hodgkin and Huxley [17] given by Keener and Sneyd [34, Chapter 5], an area of  $1\text{cm}^2$  of axon is modelled. Figure 9 shows the bond graph representation of the Hodgkin-Huxley model, consisting of three ion channels (displayed in Figure 8) together with the

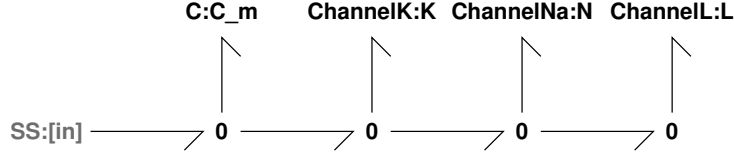


Figure 9: Membrane model

	$K^+$	$Na^+$
Internal	397	50
External	20	437

Table 3: Concentrations used in simulation (mM) [34, Table 2.1]

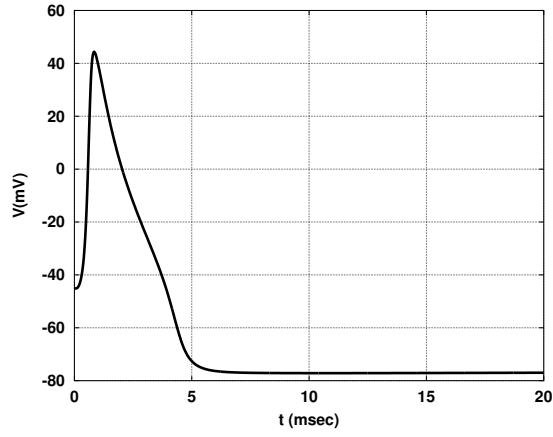
electrogenic capacitor. These four components share the same electrogenic potential and thus are connected to **0** junctions.

The model has 13 states compared to the 4 states of the HH model. For direct comparison with the HH model, the six states corresponding the internal and external amounts (concentrations) of  $K^+$ ,  $Na^+$  and  $L$  were fixed at constant values by applying appropriate external flows. Using stoichiometric analysis, the remaining conserved moieties reduce the number of independent states to 4 – the same as the original Hodgkin-Huxley model. Using the pore and gate equations developed in § 2 and § 3, together with the parameters given by Keener and Sneyd [34, Chap. 5] the reduced order system equations [5, (3.48)] were implemented numerically. The model flows were scaled by a factor of  $10^{-9}$  within the simulation for numerical reasons. The membrane was initially disturbed from the resting potential by a depolarisation of 20mV. The internal and external concentrations are taken from Keener and Sneyd [34, Table 2.1] and are given in Table 3.

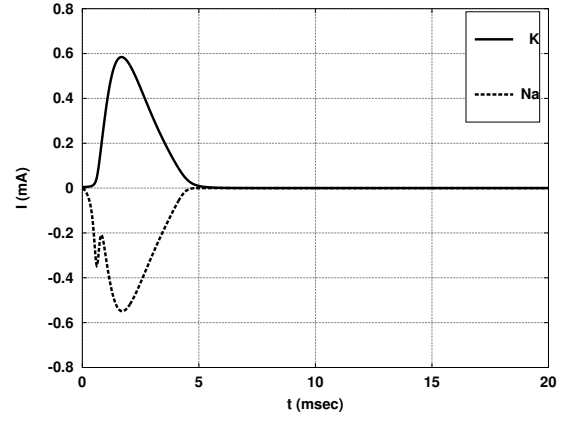
Figure 10 shows the response in the electrical domain. As shown by the discrepancies in Figures 5 and 7, the physically-based models are not identical to the original Hodgkin-Huxley model. Therefore there is a slight discrepancy between the simulation results of Figure 10 and those shown by Keener and Sneyd [34, Chap. 5], particularly after 5 ms. Hence the results in the sequel correspond to the physically-based approximation to the Hodgkin-Huxley model rather than to the original Hodgkin-Huxley model. More generally, the energetic consequences of different sets of parameters for the physically-based model, or of more complex physically-based models, could equally well be examined by the methods of this section.

In order to calculate the energy flows associated with these ionic movements, Gawthrop et al. [6] give formulae for the energy flows in the bond graph of biochemical networks. As noted above, the rate of energy transfer, or power flow, of a bond can be calculated as the product of effort and flow. Thus, the power flow associated with substance  $A$  is  $p_A = \mu_A v_A$  W where  $\mu_A$  is the chemical potential defined in Equation (3) and  $v_A$  is the molar flow rate. In the particular case relevant here that substance  $A$  occurs on each side of a membrane and is replaced on one side, and removed at the other, at a variable rate  $v_A$  so that it remains at a fixed concentration on each side, the net external power associated with substance  $A$  is:

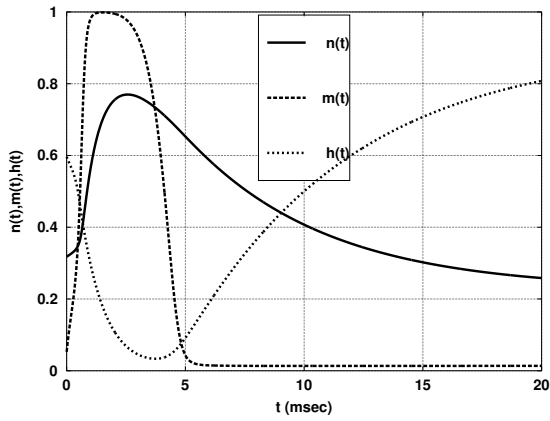
$$p_{eA} = (\mu_i - \mu_r) v_A \quad (50)$$



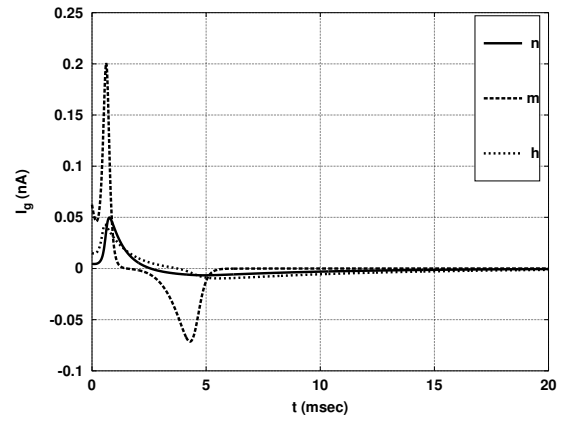
(a) Voltage:  $V$  mV



(b)  $I_k$  &  $I_n$   $\mu\text{A cm}^{-2}$



(c) Gating functions



(d) Gate current:  $I_g$   $\text{nA cm}^{-2}$

Figure 10: Membrane response: electrical domain. (a) The membrane voltage (mV) is plotted against time (msec) for a single action potential. (b) The corresponding channel currents  $I_k$  &  $I_n$  ( $\mu\text{A cm}^{-2}$ ). (c) The corresponding three gating functions  $n$ ,  $m$  and  $h$ . (d) The gate currents for the three gates ( $\text{nA cm}^{-2}$ ).

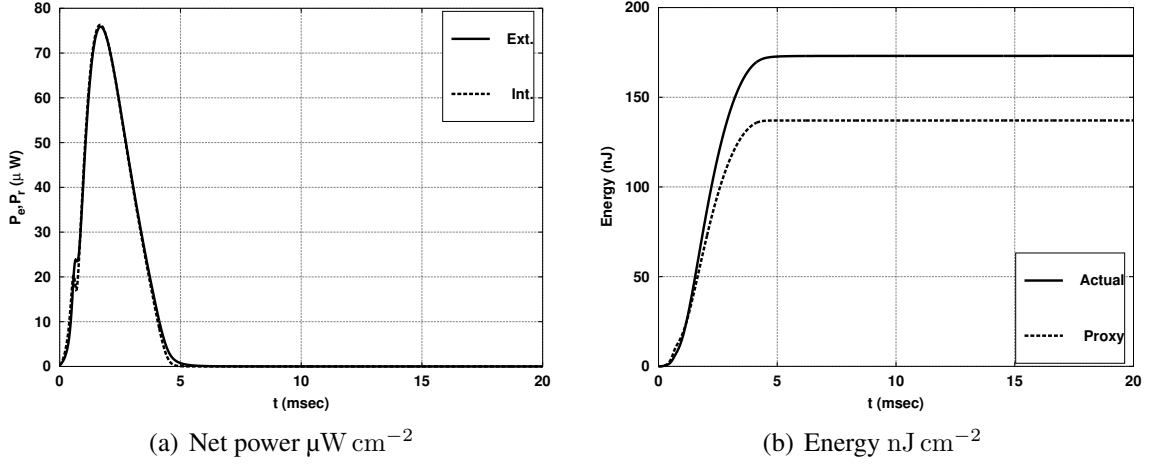


Figure 11: Power & Energy plotted against time (msec). (a) The net external power and dissipated power ( $\mu\text{W cm}^{-2}$ ). (b) The external energy (time integral of external power) and the ATP-proxy energy ( $\text{nJ cm}^{-2}$ ).

where  $\mu_i$  and  $\mu_r$  are the internal and external chemical potentials respectively. Using Equation (3)

$$\begin{aligned}\mu_i - \mu_r &= RT (\ln \chi_i - \ln \chi_r) = RT \ln \frac{\chi_i}{\chi_r} \\ &= RT \ln \frac{c_i}{c_r} = G_A\end{aligned}\quad (51)$$

where  $c_i$  and  $c_r$  are the internal and external concentrations of substance  $A$ ;  $G_A$  can be interpreted as the Gibbs free energy change of moving  $A$  from inside to outside in this particular case.

In the case of the  $i$ th chemical reaction component, the energy inflow is the product of the reaction flow  $v_i$  and the forward affinity  $A_i^f$  of Equation (12) and the energy flow out is the product of the reaction flow  $v_i$  and the reverse affinity  $A_i^r$  of Equation (13). Thus the power dissipated in the  $i$ th chemical reaction is:

$$p_i = A_i^f v_i - A_i^r v_i = A_i v_i \quad (52)$$

where the reaction affinity  $A_i$  is given by  $A_i = A_i^f - A_i^r$ .

Using the same simulation data as Figure 10, Figure 11(a) shows the external power ( $P_e \mu\text{W cm}^{-2}$ ) due to the flows of  $\text{K}^+$  and  $\text{Na}^+$  required to keep the concentrations constant and the net rate of energy dissipation ( $P_r \mu\text{W cm}^{-2}$ ). These two powers are approximately the same; the difference is due to transient energy storage in the electrogenic capacitor. The corresponding energy  $E_e(t)$  of an action potential is computed by integrating the external power  $P_e$  with respect to time

$$E_e(t) = \int_0^t P_e(\tau) d\tau \quad (53)$$

$E_e(t)$  is plotted in Figure 11(b) with the legend “Actual”; the total energy required for this particular model is about  $173 \text{ nJ cm}^{-2}$ .<sup>1</sup>

It is interesting to compare this precise method of computing energy dissipation with the ATP proxy approach. The influx of  $\text{Na}^+$  [20–22, 24] is often taken as a proxy for energy consumption. For example, as discussed by Smith and Crampin [37] and Hasenstaub et al. [21],  $3\text{Na}^+$  ions are moved back across the membrane using 1 ATP molecule by the sodium-potassium pump ( $\text{Na}^+$ ,  $\text{K}^+$ , ATPase). Thus the total  $\text{Na}^+$  passing through the membrane during an action potential  $x_n$  can be taken as a proxy for energy consumption. For example, Hasenstaub et al. [21] use the *ATP-proxy*  $x_a$  via the formula  $x_a = \frac{x_n}{3}$ . The energy corresponding to the ATP-proxy  $x_a$  can be computed from

$$E_a = G_{ATP} x_a \quad (54)$$

where  $G_{ATP} \approx 31 \text{ kJ mol}^{-1}$  is the Gibbs free energy associated with the reaction  $ATP \rightleftharpoons ADP + P_i$ .  $E_a$  is plotted in Figure 11(b) together with the actual energy  $E_e$ ; the ATP-proxy energy required for this particular model is about  $137 \text{ nJ cm}^{-2}$  – a discrepancy of about 20% which is discussed in the sequel. Alternatively, this energy requirement could be reexpressed in units of moles of *ATP* by dividing  $E_e$  and  $E_a$  by  $G_{ATP}$ .

Different physically-based action potential models will have different discrepancies between the ATP proxy approach and the actual energy. Thus comparing action potential energy requirements of different models (whether physically-based or non-physically-based) using the ATP proxy approach may be misleading.

## 5 Energy consumption in healthy and degenerative retinal ganglion cells

	Experiments		Simulations
<b>WT mice</b>	mean	std	
Vmax [mV]	23	6	23
Spike Width [ms]	1.9	0.8	2
<b>RD1 mice</b>	mean	std	
Vmax [mV]	29	9	28
Spike Width [ms]	1.5	0.5	1.6

Table 4: Comparison of the experimental data (n=8 for WT and n=6 for RD cells) and simulation results. Mean values and standard errors are given for the experiments. Results are shown using standard ionic model formulation.

As discussed in Appendix A, *in vitro* data was collected and analysed from retinal ganglion cells (RGCs) of wild-type (WT) and degenerative (RD1) mice. Figure 12(a) illustrates that the experimentally recorded action potentials belong to separate topological manifolds

<sup>1</sup> The energy corresponding to the initial depolarisation of  $V_0 = 20\text{mV}$  is  $\frac{1}{2}C_m V_0^2 = 0.2\text{nJ cm}^{-2}$ ; this can be neglected in the overall energy balance.

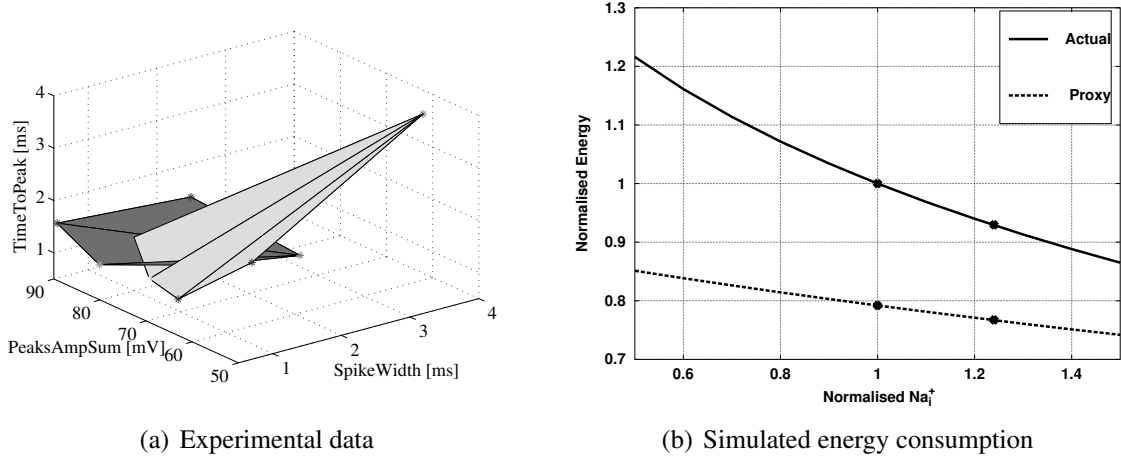


Figure 12: Retinal Ganglion Cells. (a) Topological manifolds for the parameters of action potentials in WT and RD1 mice. Pale: WT mice; dark: RD1 mice. TimeToPeak is calculated as a difference between the time of the maximum amplitude of an action potential and the time taken for the membrane potential to reach  $dV/dt > 10$  mV/ms threshold. PeaksAmpSum is calculated as a sum of the maximum amplitude of an action potential and absolute hyperpolarisation level. (b) Simulated Energy consumption as internal  $\text{Na}^+$  concentration varies: the ratio of the energy consumption to the actual energy consumption at the nominal internal  $\text{Na}_i^+$  concentration  $\text{Na}_0^+$  is plotted against  $\text{Na}_i^+/\text{Na}_0^+$  for both actual and proxy energy consumption.

for WT and RD1 mice. This suggests that energy consumption for single action potentials is different for WT and RD1 mice.

The methodology employed here to account for differences in the shape of action potential in WT and RD1 cells assumes that sodium and potassium conductances contribute the most to the spike width and spike maximum amplitude. Other conductances may also contribute to the shape of the action potential; however, their effect was not investigated here. Due to sodium conductance contributing maximally to the amplitude of action potentials, this conductance may be overestimated for RD1 cells that have larger mean spike height. This does not affect the qualitative results presented here, but is a possible limitation for the interpretation of quantitative results.

Using experimentally fitted parameters as described in the Supporting Material, simulations of both cell types were conducted and a comparison of the experimental data and simulation results is given in Table 4.

The simulation results indicated that  $\bar{g}_{\text{Na}}$  is increased by at least 24% in degenerative retina. Figure 12(b) shows how actual and ATP-proxy energy varies with internal sodium concentration. The solid line illustrates actual energy consumption, the dashed line illustrates the ATP-proxy calculation, and the crosses indicate data points calculated for RD1 and WT mice energy consumption. Figure 12(b) illustrates that the difference in the normalised energy consumption for one action potential between WT and RD1 RGCs is 0.03 using ATP-proxy methodology, while the difference is 0.08 using methodology proposed in this paper. The figure shows that the ATP-proxy methodology underestimates the energy

consumption for both mouse types. In addition, the ATP-proxy methodology underestimates the difference between the two types of mice, while the proposed methodology provides accurate comparison of energy consumption between two similar-shaped action potentials (note the relatively small differences between WT and RD1 cells in Table 4).

## 6 DISCUSSION

	$K^+$	$Na^+$	$K^+ + Na^+$	ATP
$x$ (pmol)	13.60	13.27	–	4.42
$G$ (kJ mol $^{-1}$ )	7.54	3.68	–	31
$E$ (nJ)	101.35	71.73	173.08	137.08

Table 5: Simulation results (per cm $^2$ ).  $x$  is the quantity,  $G$  the molar free energy and  $E$  the energy consumed by the action potential.  $x_a$  is computed from the formula  $x_a = \frac{x_n}{3}$

We have extended our earlier work on energy-based bond graph modelling of biochemical systems to encompass chemoelectrical systems. In particular, we have introduced the electrogenic capacitor and the electrostoichiometric transformer to bridge the chemical and electrical domains.

As a particular example illustrating the general approach, we have constructed a bond graph model of the Hodgkin and Huxley [17] model of the axon; and we have used this model to show that calculation of energy consumption during generation of the action potential by counting  $Na^+$  ions crossing the membrane underestimates true energy consumption by around 20%.

In this particular situation, the concentrations are constant and thus Equation (51) is appropriate. Moreover, the contribution of the leakage and the gating currents are small and can be neglected. The values of Table 3 and Equation (51) gives the molar free energy values of Table 5 for  $K^+$ ,  $Na^+$ ; that for ATP is taken from Keener and Sneyd [34, (1.23)]. Because the actual energy consumption depends on both the amounts of  $K^+$ ,  $Na^+$  as well as on the internal and external concentrations, there is no way that the ATP-proxy formula (based on only the amount of  $Na^+$ ) can give the correct value under all circumstances. To illustrate this, Figure 12 shows how actual and ATP-proxy energy varies with internal  $Na^+$  concentration expressed as a ratio  $\rho$  to the nominal concentration of Table 3. The discrepancy between actual and ATP-proxy energy varies with  $\rho$ . Moreover, the method of this paper does *not* require the concentrations to be constant during an action potential and is thus applicable to more general situations.

The wider significance of our approach is that it provides a framework within which biophysically based models are robustly thermodynamically compliant [6], as required for example when considering the energetic costs and consequences of cellular biological processes. Furthermore, the Bond Graph approach provides a basis for modular modelling of large, multi-domain electro-chemical biological systems, such as is now commonplace in systems biology models of excitable membranes in the neuronal and cardiac contexts. Components and modules which are represented as Bond Graphs are physically plausible models which obey the basic principles of thermodynamics, and therefore larger models

constructed from such modules will also consequentially be physically plausible models. Future work will further develop these concepts in order to represent ligand-gated ion channels, ion pumps (such as the  $\text{Ca}^{2+}$  pump SERCA [5, 38] and the  $\text{Na}^{+}$  pump [37, 39], as are required for current generation neuronal and cardiac cell models. This modular approach allows simpler modules to be replaced by more complex modules, or empirical modules to be replaced by physically-based modules, as the underlying science advances.

Furthermore, the multi-domain nature of Bond Graphs makes possible extension of the approach to mechano-chemical transduction. In actively contracting cardiac muscle, for example, energetic considerations are dominated by force production, where approximately 75–80% of ATP consumption in cardiomyocytes over a cardiac cycle is due to formation of contractile cross-bridges, 5–10% due to the  $\text{Na}^{+}$  pump, and  $\text{Ca}^{2+}$  extrusion and uptake into  $\text{Ca}^{2+}$  stores accounting for the remainder [40]. In cardiac muscle, energetics is known to play a critical role in the health of cardiac muscle, with many studies implicating energetic imbalance or inadequacy of energy production in heart disease [41]. Models which provide a mechanism with which to assess the energetic aspects of cell function are therefore much needed. Combining metabolism, electro-chemical and chemo-mechanical energy transduction to examine energy flows within the heart [41, 42] is therefore a major goal of our work. Conservation of mass and energy have been used by Wei et al. [43] and Ullah et al. [44] to examine the dynamics of seizure and spreading depression. It would be interesting to reexamine this work in the more general context of bond graph modelling.

The ATP-proxy approach is based on assuming that the biological entity is operating in a normal state and therefore could lead to misleading conclusions in a pathophysiological state. In contrast, our approach makes no assumption of normality and may be expected to be of use in pathophysiological states in general and, in particular, the retinal example discussed in this paper. Our use of the RD1 degenerate retina mouse model ensures that the outcomes of this project are directly relevant to human patients since RD1 mice have a degenerate retina that has distinct similarities to that observed in human patients with *retinitis pigmentosa* – a set of hereditary retinal diseases that results from the degenerative loss of the photoreceptors in the retina. It has been proposed that the death of rod photoreceptors results in decreased oxygen consumption [45]. In addition, it has been shown that potassium channel-opening agents directly affect mitochondria [46]. Therefore, it is important to understand how energy consumption in degenerative retina is altered. The proposed methodology allows a comparison between the energy consumption in healthy and degenerate mice, even when the differences in action potentials between the two types are small.

The modularity of the bond graph approach allows the action potential models of this paper to be combined with models of the various trans-membrane pumps and transporters to give a thermodynamically correct model of ATP consumption. It would therefore be interesting to reexamine the optimality arguments of Hasenstaub et al. [21] and Sengupta and Stemmler [24] using this approach.

As shown by Mitchell [47, 48], the key feature of mitochondria is *chemiosmotic* energy transduction whereby a chain of redox reactions pumps protons across the mitochondrial inner membrane to generate the *proton-motive force* (PMF). This PMF is then used to power the production of ATP – the universal fuel of living systems. The ideas expressed in this paper have been recently extended to model chemiosmotic energy transduction [49]. Future work will combine the chemoelectrical bond graph models of this paper with bond graph



models of anaerobic metabolism [6], and bond graph models of mitochondrial chemiosmotic energy transduction [49], to give integrated models of neuronal energy transduction suitable for investigating neuronal dysfunctions such as Parkinson’s disease [28, 29, 50].

## 7 ACKNOWLEDGEMENTS

We would like to thank the reviewers for their suggestions for improving the paper. P.G. would like to thank the Melbourne School of Engineering for its support via a Professorial Fellowship. I.S. gratefully acknowledges funding from Sonderforschungsbereich (SFB) 803, project Z02 (Deutsche Forschungsgemeinschaft, Germany). This research was in part conducted and funded by the Australian Research Council Centre of Excellence in Convergent Bio-Nano Science and Technology (project number CE140100036).

## 8 AUTHOR CONTRIBUTIONS

The theory was developed by PJG, IS and EC. The theoretical part of the paper was written by PJG, IS and EC and the experimental part by TK. Experiments were conducted by SS and MI.

## 9 DATA ACCESSIBILITY

A virtual reference environment [32] is available for this paper at [https://github.com/uomsystemsbiology/energetic\\_cost\\_reference\\_environment](https://github.com/uomsystemsbiology/energetic_cost_reference_environment).

## 10 References

### References

- [1] Peter Atkins and Julio de Paula. *Physical Chemistry for the Life Sciences*. Oxford University Press, 2nd edition, 2011. 3, 6
- [2] H. M. Paynter. *Analysis and design of engineering systems*. MIT Press, Cambridge, Mass., 1961. 3
- [3] George Oster, Alan Perelson, and Aharon Katchalsky. Network thermodynamics. *Nature*, 234:393–399, December 1971. doi: 10.1038/234393a0. 3, 6, 10
- [4] George F. Oster, Alan S. Perelson, and Aharon Katchalsky. Network thermodynamics: dynamic modelling of biophysical systems. *Quarterly Reviews of Biophysics*, 6(01): 1–134, 1973. doi: 10.1017/S0033583500000081. 6, 7, 10

- [5] Peter J. Gawthrop and Edmund J. Crampin. Energy-based analysis of biochemical cycles using bond graphs. *Proceedings of the Royal Society A: Mathematical, Physical and Engineering Science*, 470(2171):1–25, 2014. doi: 10.1098/rspa.2014.0459. Available at arXiv:1406.2447. 6, 7, 8, 10, 18, 24
- [6] Peter J. Gawthrop, Joseph Cursons, and Edmund J. Crampin. Hierarchical bond graph modelling of biochemical networks. *Proceedings of the Royal Society A: Mathematical, Physical and Engineering Sciences*, 471(2184):1–23, 2015. ISSN 1364-5021. doi: 10.1098/rspa.2015.0642. Available at arXiv:1503.01814. 18, 23, 25
- [7] P. J. Gawthrop and E. J. Crampin. Modular bond-graph modelling and analysis of biomolecular systems. *IET Systems Biology*, 10(5):187–201, October 2016. ISSN 1751-8849. doi: 10.1049/iet-syb.2015.0083. Available at arXiv:1511.06482.
- [8] Peter J. Gawthrop. Bond-graph modelling and causal analysis of biomolecular systems. In Wolfgang Borutzky, editor, *Bond Graphs for Modelling, Control and Fault Diagnosis of Engineering Systems*, pages 587–623. Springer International Publishing, Berlin, 2017. ISBN 978-3-319-47434-2. doi: 10.1007/978-3-319-47434-2\_16. 3
- [9] P. J. Gawthrop and L. P. S. Smith. *Metamodelling: Bond Graphs and Dynamic Systems*. Prentice Hall, Hemel Hempstead, Herts, England., 1996. ISBN 0-13-489824-9. 3
- [10] Amalendu Mukherjee, Ranjit Karmaker, and Arun Kumar Samantaray. *Bond Graph in Modeling, Simulation and Fault Identification*. I.K. International, New Delhi., 2006. 3
- [11] Wolfgang Borutzky. *Bond Graph Modelling of Engineering Systems: Theory, Applications and Software Support*. Springer, 2011. ISBN 9781441993670. 3
- [12] Dean C Karnopp, Donald L Margolis, and Ronald C Rosenberg. *System Dynamics: Modeling, Simulation, and Control of Mechatronic Systems*. John Wiley & Sons, 5th edition, 2012. ISBN 978-0470889084. 3
- [13] Peter J Gawthrop and Geraint P Bevan. Bond-graph modeling: A tutorial introduction for control engineers. *IEEE Control Systems Magazine*, 27(2):24–45, April 2007. doi: 10.1109/MCS.2007.338279. 3
- [14] F. E. Cellier. *Continuous system modelling*. Springer-Verlag, 1991. 3
- [15] J. Greifeneder and F.E. Cellier. Modeling chemical reactions using bond graphs. In *Proceedings ICBGM12, 10th SCS Intl. Conf. on Bond Graph Modeling and Simulation*, pages 110–121, Genoa, Italy, 2012. 3, 10
- [16] Dean Karnopp. Bond graph models for electrochemical energy storage : electrical, chemical and thermal effects. *Journal of the Franklin Institute*, 327(6):983 – 992, 1990. ISSN 0016-0032. doi: 10.1016/0016-0032(90)90073-R. 3, 8
- [17] A. L. Hodgkin and A. F. Huxley. A quantitative description of membrane current and its application to conduction and excitation in nerve. *The Journal of Physiology*, 117 (4):500–544, 1952. 3, 4, 10, 11, 15, 17, 23

- [18] Bertil Hille. *Ion Channels of Excitable Membranes*. Sinauer Associates, Sunderland, MA, USA, 3rd edition, 2001. ISBN 978-0-87893-321-1. 3, 15
- [19] Mathieu Cloutier, B. Bolger, Fiachra, P. Lowry, John, and Peter Wellstead. An integrative dynamic model of brain energy metabolism using in vivo neurochemical measurements. *Journal of Computational Neuroscience*, 27(3):391–414, 2009. ISSN 0929-5313. doi: 10.1007/s10827-009-0152-8. 3
- [20] Brett C. Carter and Bruce P. Bean. Sodium entry during action potentials of mammalian neurons: Incomplete inactivation and reduced metabolic efficiency in fast-spiking neurons. *Neuron*, 64(6):898 – 909, 2009. ISSN 0896-6273. doi: 10.1016/j.neuron.2009.12.011. 21
- [21] Andrea Hasenstaub, Stephani Otte, Edward Callaway, and Terrence J. Sejnowski. Metabolic cost as a unifying principle governing neuronal biophysics. *Proceedings of the National Academy of Sciences*, 107(27):12329–12334, 2010. doi: 10.1073/pnas.0914886107. 3, 21, 24
- [22] Biswa Sengupta, Martin Stemmler, Simon B. Laughlin, and Jeremy E. Niven. Action potential energy efficiency varies among neuron types in vertebrates and invertebrates. *PLoS Comput Biol*, 6(7):e1000840, 07 2010. doi: 10.1371/journal.pcbi.1000840. 21
- [23] Biswa Sengupta, Martin B. Stemmler, and Karl J. Friston. Information and efficiency in the nervous system synthesis. *PLoS Comput Biol*, 9(7):e1003157, 07 2013. doi: 10.1371/journal.pcbi.1003157.
- [24] B. Sengupta and M.B. Stemmler. Power consumption during neuronal computation. *Proceedings of the IEEE*, 102(5):738–750, May 2014. ISSN 0018-9219. doi: 10.1109/JPROC.2014.2307755. 21, 24
- [25] Jeremy E Niven. Neuronal energy consumption: biophysics, efficiency and evolution. *Current Opinion in Neurobiology*, 41:129 – 135, 2016. ISSN 0959-4388. doi: 10.1016/j.conb.2016.09.004. 3
- [26] Jeremy E. Niven and Simon B. Laughlin. Energy limitation as a selective pressure on the evolution of sensory systems. *Journal of Experimental Biology*, 211(11):1792–1804, 2008. ISSN 0022-0949. doi: 10.1242/jeb.017574. 3
- [27] M. Flint Beal. Does impairment of energy metabolism result in excitotoxic neuronal death in neurodegenerative illnesses? *Annals of Neurology*, 31(2):119–130, 1992. ISSN 1531-8249. doi: 10.1002/ana.410310202. 3
- [28] Peter Wellstead. *A New Look at Disease: Parkinson’s through the eyes of an engineer*. Control Systems Principles, Stockport, UK, 2012. ISBN 978-0-9573864-0-2. 3, 25
- [29] Peter Wellstead and Mathieu Cloutier, editors. *Systems Biology of Parkinson’s Disease*. Springer New York, 2012. ISBN 978-1-4614-3411-5. doi: 10.1007/978-1-4614-3411-5. 25

- [30] M. Cloutier, R. Middleton, and P. Wellstead. Feedback motif for the pathogenesis of Parkinson’s disease. *Systems Biology, IET*, 6(3):86–93, June 2012. ISSN 1751-8849. doi: 10.1049/iet-syb.2011.0076.
- [31] Amy K. Reeve, Eve M. Simcox, Michael R. Duchen, and Doug M. Turnbull, editors. *Mitochondrial Dysfunction in Neurodegenerative Disorders*. Springer, Switzerland, 2nd edition, 2016. ISBN 978-3-319-28637-2. 3
- [32] Daniel G. Hurley, David M. Budden, and Edmund J. Crampin. Virtual reference environments: a simple way to make research reproducible. *Briefings in Bioinformatics*, 2014. doi: 10.1093/bib/bbu043. 5, 25
- [33] Pierre Van Rysselberghe. Reaction rates and affinities. *The Journal of Chemical Physics*, 29(3):640–642, 1958. doi: 10.1063/1.1744552. 7
- [34] James P Keener and James Sneyd. *Mathematical Physiology: I: Cellular Physiology*, volume 1. Springer, 2nd edition, 2009. 11, 12, 13, 15, 17, 18, 23
- [35] Christof Koch. *Biophysics of computation: information processing in single neurons*. Oxford University Press, Oxford, 2004. 12
- [36] David Sterratt, Bruce Graham, Andrew Gillies, and David Willshaw. *Principles of Computational Modelling in Neuroscience*. Cambridge University Press, 2011. ISBN 9780521877954. 12
- [37] N.P. Smith and E.J. Crampin. Development of models of active ion transport for whole-cell modelling: cardiac sodium-potassium pump as a case study. *Progress in Biophysics and Molecular Biology*, 85(2-3):387 – 405, 2004. doi: 10.1016/j.pbiomolbio.2004.01.010. 21, 24
- [38] Kenneth Tran, Nicolas P. Smith, Denis S. Loiselle, and Edmund J. Crampin. A thermodynamic model of the cardiac sarcoplasmic/endoplasmic Ca<sup>2+</sup> (SERCA) pump. *Biophysical Journal*, 96(5):2029 – 2042, 2009. ISSN 0006-3495. doi: 10.1016/j.bpj.2008.11.045. 24
- [39] Jonna R. Terkildsen, Steven Niederer, Edmund J. Crampin, Peter Hunter, and Nicolas P. Smith. Using physiome standards to couple cellular functions for rat cardiac excitation-contraction. *Experimental Physiology*, 93(7):919–929, 2008. ISSN 1469-445X. doi: 10.1113/expphysiol.2007.041871. 24
- [40] Kenneth Tran, Denis S. Loiselle, and Edmund J. Crampin. Regulation of cardiac cellular bioenergetics: mechanisms and consequences. *Physiological Reports*, 3(7):e12464, 2015. ISSN 2051-817X. doi: 10.14814/phy2.12464. 24
- [41] Stefan Neubauer. The failing heart – an engine out of fuel. *New England Journal of Medicine*, 356(11):1140–1151, 2007. doi: 10.1056/NEJMra063052. 24
- [42] Arnold M Katz. *Physiology of the Heart*. Lippincott Williams and Wilkins, Philadelphia, fifth edition, 2011. ISBN 978-1-60831-171-2. 24

- [43] Yina Wei, Ghanim Ullah, and Steven J Schiff. Unification of neuronal spikes, seizures, and spreading depression. *The Journal of Neuroscience*, 34(35):11733–11743, 2014. doi: 10.1523/JNEUROSCI.0516-14.2014. 24
- [44] Ghanim Ullah, Yina Wei, Markus A Dahlem, Martin Wechselberger, and Steven J Schiff. The role of cell volume in the dynamics of seizure, spreading depression, and anoxic depolarization. *PLoS Comput Biol*, 11(8):e1004414, 08 2015. doi: 10.1371/journal.pcbi.1004414. 24
- [45] JiKui Shen, Xiaoru Yang, Aling Dong, Robert M. Petters, You-Wei Peng, Fulton Wong, and Peter A. Campochiaro. Oxidative damage is a potential cause of cone cell death in retinitis pigmentosa. *Journal of Cellular Physiology*, 203(3):457–464, 2005. ISSN 1097-4652. doi: 10.1002/jcp.20346. 24
- [46] Bogusz Kulawiak, Alexei P. Kudin, Adam Szewczyk, and Wolfram S. Kunz. BK channel openers inhibit ROS production of isolated rat brain mitochondria. *Experimental Neurology*, 212(2):543 – 547, 2008. ISSN 0014-4886. doi: <http://dx.doi.org/10.1016/j.expneurol.2008.05.004>. 24
- [47] Peter Mitchell. Possible molecular mechanisms of the protonmotive function of cytochrome systems. *Journal of Theoretical Biology*, 62(2):327–367, 1976. doi: 10.1016/0022-5193(76)90124-7. 24
- [48] Peter Mitchell. Chemiosmotic coupling in oxidative and photosynthetic phosphorylation. *Biochimica et Biophysica Acta (BBA) - Bioenergetics*, 1807(12):1507 – 1538, 2011. ISSN 0005-2728. doi: 10.1016/j.bbabo.2011.09.018. Special Section: Peter Mitchell - 50th anniversary of the chemiosmotic theory. 24
- [49] Peter Gawthrop. Bond Graph Modelling of Chemiosmotic Biomolecular Energy Transduction. *IEEE Transactions on NanoBioscience*, 2017. doi: 10.1109/TNB.2017.2674683. In press. 24, 25
- [50] Peter Wellstead and Mathieu Cloutier. An energy systems approach to Parkinson’s disease. *Wiley Interdisciplinary Reviews: Systems Biology and Medicine*, 3(1):1–6, 2011. ISSN 1939-005X. doi: 10.1002/wsbm.107. 25
- [51] Tatiana Kameneva, Hamish Meffin, and AnthonyN. Burkitt. Modelling intrinsic electrophysiological properties of on and off retinal ganglion cells. *Journal of Computational Neuroscience*, 31(3):547–561, 2011. ISSN 0929-5313. doi: 10.1007/s10827-011-0322-3. 31

## A Application of the proposed methodology to calculate the energy consumption in healthy and degenerative retinal ganglion cells

*In vitro* data was collected and analysed from retinal ganglion cells (RGCs) of wild-type (WT) (n=8) and degenerative RD1 (n=6) mice 4 - 4.5 month old. Experimental procedures were approved by the animal welfare committee at the University of Melbourne and are in accordance with local and national guidelines for animal care. Animals were housed in temperature-regulated facilities on a 12h light/dark cycle in the animal house and had plentiful access to food and water. Neither WT nor RD1 mice were dark adapted for these experiments.

Retinae from WT and RD1 mice were treated identically. Mice were anaesthetised with simultaneous ketamine (67 mg/kg) and xylazine (13 mg/kg) injections, the eyes were enucleated and then the mice were killed by cervical dislocation. Their eyes were bathed in carbogenated (95% O<sub>2</sub> and 5% CO<sub>2</sub>) Ames' medium (Sigma-Aldrich, St. Louis, MO), hemisected at the ora serata, and the cornea and lens were removed. The retina was continuously superfused with carbogenated Ames medium at a rate of 4-8 ml/min. All of the procedures were performed at room temperature and in normal room light.

The flat-mount retina was viewed through the microscope with the use of Nomarski DIC optics and also on a video monitor with additional 4x magnification using a CCD camera (Ikegami, ICD-48E). For whole cell recording, a small opening was first made with a sharp tip pipette (resistance above 14 M $\Omega$ ) through the inner limiting membrane and optic fibre layer that covered a selected retinal ganglion cell. Prior to recording, the pipette voltage in the bath was nullified. The pipette series resistance was measured and compensated for using standard amplifier circuitry (SEC-05x; NPI Electronic Instruments). Pipette resistance was in the range of 7-14 M $\Omega$  for all experiments. Membrane potentials were amplified (as above with SEC-05x, npi) and digitised at 50 kHz (USB-6221, National Instruments), acquired and stored in digital form by custom software developed in Matlab (Mathworks).

In this study, we sought to account for the differences in the energy consumption between WT and RD1 RGCs on the basis of differences in the magnitudes of the maximal conductance of sodium and potassium currents,  $\bar{g}_{Na}$  and  $\bar{g}_K$  respectively. While all other parameters were kept fixed,  $\bar{g}_{Na}$  and  $\bar{g}_K$  were systematically varied in the range  $[10^{-15}, 0.1]$  in variable steps (higher resolution for smaller values). For conservative calculation of the difference in the energy consumption, the smallest difference between  $\bar{g}_{Na}$  and  $\bar{g}_K$  in WT and RD1 types that replicated experimental data is reported here. Model parameters used in simulations are given in Table 5;  $\bar{g}_i$ ,  $V_i$  are maximum conductance and reversal potential of the current "i".  $V_{Ca}$  and  $\bar{g}_{K(Ca)}$  depend on the intracellular Ca<sup>2+</sup> concentration. At the moment, no experimental data is available on the properties of gating parameters for RGS in RD1 mice. Due to this, the same gating parameters were used to model action potential in healthy and degenerative tissue. A single-compartment Hodgkin-Huxley type neurons was simulated in NEURON. The standard Euler integration method was used in simulations. Data was analysed in Matlab (Mathworks).

Table 5. Simulation parameters.

$T = 22^0 \text{ C}$	$C_m = 1 \mu \text{ F/cm}^2$	The following simula-
$V_{\text{Na}} = 35 \text{ mV}$	$\bar{g}_{\text{Na}}$ is varied in simulations	
$V_{\text{Ca}}$ is variable, refer to [51]	$\bar{g}_{\text{Ca}} = 2.2 \cdot 10^{-3} \text{ S/cm}^2$	
$V_{\text{K}} = -70 \text{ mV}$	$\bar{g}_{\text{K}}$ is varied in simulations	
	$\bar{g}_{\text{K,A}} = 3.6 \cdot 10^{-2} \text{ S/cm}^2$	
	$\bar{g}_{\text{K(Ca)}}$ is variable, refer to [51]	
$V_{\text{L}} = -60 \text{ mV}$	$\bar{g}_{\text{L}} = 10^{-6} \text{ S/cm}^2$	
$V_{\text{h}} = 0 \text{ mV}$	$\bar{g}_{\text{h}} = 10^{-7} \text{ S/cm}^2$	
$V_{\text{T}} = 120 \text{ mV}$	$\bar{g}_{\text{T}} = 10^{-3} \text{ S/cm}^2$	

tion parameters reproduced the maximum amplitude and width of the experimentally recorded action potentials in WT and RD1 mice and gave the smallest difference in values between the two retina types. Parameters for WT:  $\bar{g}_{\text{Na}} = 0.0342 \text{ S/cm}^2$ ,  $\bar{g}_{\text{K}} = 0.0102 \text{ S/cm}^2$ . Parameters for RD1:  $\bar{g}_{\text{Na}} = 0.0422 \text{ S/cm}^2$ ,  $\bar{g}_{\text{K}} = 0.0102 \text{ S/cm}^2$ .